GPS Solutions (2023) 27:100
https://doi.org/10.1007/s10291-023-01443-3

ORIGINAL ARTICLE

Inter-system biases solution strategies in multi-GNSS kinematic precise point positioning

Mowen Li[1,2] · Adria Rovira-Garcia[2] · Wenfeng Nie[1,3] · Tianhe Xu[1,3] · Guochang Xu[1,4]

Received: 5 March 2022 / Accepted: 20 March 2023 / Published online: 6 April 2023

Abstract

Estimating inter-system biases (ISBs) is important in multi-constellation Global Navigation Satellite System (GNSS) processing. The present study aims to evaluate and screen out an optimal estimation strategy of ISB for multi-GNSS kinematic precise point positioning (PPP). The candidate strategies considered for ISB estimation are white noise process (ISB-WN), random walk process (ISB-RW), constant (ISB-CT) and eliminated by between-satellite single-differenced observations (ISB-SD). We first present the mathematical model of ISB derived from the observation combination among different GNSSs, and we demonstrate the equivalence between ISB-WN and ISB-SD in the Kalman filter. In order to evaluate the performance of these four ISB solution strategies, we implement kinematic PPP with 1-month static data from 112 International GNSS service stations and two-hour dynamic vehicular data collected in an urban case. For comparison, precise orbit and clock products from the Center for Orbit Determination in Europe (CODE), GeoForschungsZentrum in Germany (GFZ) and Wuhan University (WHU) are employed in our experiments. The results of static tests show that the positioning accuracy is comparable among the four strategies, but ISB-CT performs slightly better in convergence time. In the kinematic test, there are more cycle slips than static test, and the ISB-CT improves the positioning accuracy by 15.7%, 38.9% and 63.2% in east, north and up components, and reduces the convergence time by 60.1% comparing with the other strategies. Moreover, both the static and kinematic tests prove the consistence among CODE, GFZ and WHU precise products and the equivalence between ISB-WN and ISB-SD strategies. Finally, more, i.e., the same amount of cycle slips as for the dynamic data, are artificially added to the static data to conduct the pseudo-kinematic test. The result shows that ISB-CT improves the positioning accuracy and convergence time by 19.2% and 24.4%, respectively.

Keywords Multi-GNSS · Inter-system bias (ISB) · Kinematic · Precise point positioning (PPP)

Introduction

Thanks to the availability of different Global Navigation Satellite Systems (GNSSs) and the International GNSS Service (IGS) Multi-GNSS Experiment (MGEX), the multi-GNSS precise point positioning (PPP) has been deeply studied and developed (Li et al. 2015; Montenbruck et al. 2017). In multi-GNSS PPP, the receiver hardware delays are different among GNSS constellations, which are called inter-system biases (ISBs) and can be estimated as the difference of receiver clock offsets between different constellations (Gao et al. 2018; Tian et al. 2018). Different strategies have been used for estimating ISBs: The constant model (ISB-CT) was proposed because of the stability of ISBs (Liu et al. 2017; Paziewski and Wielgosz 2015); the white noise model (ISB-WN) was adopted in real-time multi-GNSS PPP (de Bakker and Tiberius 2017) and the random walk process (ISB-RW) was first proposed in GPS/GLONASS PPP by Li and Zhang (2014).

The characteristics of ISB estimates using different precise MGEX products for permanent stations have been investigated in recent years. Jiang et al. (2019) assessed

✉ Wenfeng Nie
wenfengnie@sdu.edu.cn

1 Institute of Space Sciences, Shandong University, Weihai, China

2 Research Group of Astronomy and Geomatics (gAGE), Universitat Politecnica de Catalunya (UPC), Barcelona, Spain

3 State Key Laboratory of Geo-Information Engineering, Xi'an, China

4 Institute of Space Science and Applied Technology, Harbin Institute of Technology, Shenzhen, China

different ISB strategies with a three-hour arc window process and concluded that ISB-RW and ISB-WN performed best with the precise products of GFZ, while the ISB-CT outperformed with the products from WHU. Liu et al. (2019) used ISB-RW with the products of GFZ, WHU and CODE for the GPS/BDS experiment. The authors found that the ISBs with GFZ products showed limited stability, while the ISBs with CODE and WHU products were more stable for a constant model. Zhou et al. (2019) set up combinations of GLONASS (R), Galileo (E), BDS (C) or QZSS ISBs with GPS (G) in kinematic PPP processing. The results showed that ISB-CT outperformed ISB-RW and ISB-WN slightly with CODE and WHU products in the positioning accuracy and convergence time. However, the ISB-CT performed worse with GFZ products. Hong et al. (2019) studied the characteristics of GLONASS, Galileo and BDS ISBs in static PPP. Considering the observed stability of ISB estimates and the strength of the observed model, the authors proposed ISB-CT for CODE and WHU products, while 20-min piecewise ISB-CT with GFZ products.

Since the strategy applied by GFZ to determine ISBs was not available in any reference, the above studies inferred that a different stochastic model rather than constant for ISBs in multi-GNSS satellite clock estimation was applied by GFZ. Thanks to the GFZ Analysis Strategy Summary published on the MGEX Data and Products page of the IGS official website (https://igs.org/mgex/data-products/#products), the current ISBs strategy applied by GFZ is clearly presented as "one bias per station per constellation," which is the same as the strategy applied by CODE (Prange et al. 2017). Moreover, a discontinuity of GFZ MGEX products in GPS week 2037 (DOY 20–26, 2019) is indicated on the same page of the IGS website; however, the precise products analyzed in Hong et al. (2019), Jiang et al. (2019), Liu et al. (2019), and Zhou et al. (2019) were all before 2019. Therefore, it is reasonable to expect that estimating ISBs as constant with GFZ precise products may perform comparably with CODE products in the multi-GNSS PPP from 2019 onwards.

So far, we have summarized the ISB estimation strategies applied by three analysis centers (ACs) as a 1-day constant for CODE and GFZ, and an arc-dependent constant for WHU (Guo et al. 2016). The next section briefly introduces ISB solution strategies in multi-GNSS kinematic PPP. Then, we detail the experimental setups based on the data from IGS MGEX stations, vehicular test and pseudo-kinematic test. The performance of ISB strategies in multi-GNSS kinematic PPP is analyzed based on the differences of ISB estimates, positioning accuracy and convergence time using the precise orbit and clock products provided by CODE, GFZ and WHU. The final section summarizes our findings.

Methodology

This study employs, for the sake of eliminating first-order ionospheric delays, the double-frequency ionosphere-free (IF) combination between observations. Thus, the ISB mathematical and stochastic models are explained in what follows, based on multi-GNSS IF observations.

ISBs in multi-GNSS PPP observations

The IF pseudo-range and carrier phase measurements at a particular epoch can be written as follows (Leick et al. 2015):

$$P_{\mathrm{IF}}^{s,j} = \rho_r^{s,j} + c\delta\tilde{t}_r^s + M_r^{s,j} \cdot \mathrm{ZWD}_r + \xi_{\mathrm{IF},r}^{s,j} \tag{1}$$

$$L_{\mathrm{IF}}^{s,j} = \rho_r^{s,j} + c\delta\tilde{t}_r^s + M_r^{s,j} \cdot \mathrm{ZWD}_r + \tilde{N}_{\mathrm{IF}}^{s,j} + \varepsilon_{\mathrm{IF},r}^{s,j} \tag{2}$$

where the superscript s denotes the GNSS constellation, indices r and j represent the receiver and satellite belonging to s. $P_{\mathrm{IF}}^{s,j}$ and $L_{\mathrm{IF}}^{s,j}$ are the IF pseudo-range and phase measurements; $\rho_r^{s,j}$ is geometric distance between receiver and satellite; c is the speed of light; $\delta\tilde{t}_r^s$ represents receiver clock offset; ZWD_r denotes the tropospheric zenith wet delay (ZWD) and $M_r^{s,j}$ is the elevation-dependent mapping function with respect to j; $\tilde{N}_{IF}^{s,j}$ denotes the IF ambiguity in the unit of meter; $\xi_{\mathrm{IF},r}^{s,j}$ and $\varepsilon_{\mathrm{IF},r}^{s,j}$ represent residuals including measurement noise and multipath effect. For brevity, some items are not explicated in (1) and (2), as clock offset and pseudo-range hardware delay of the satellite can be obtained from products; receiver hardware delay and satellite phase hardware delay can be absorbed by $\delta\tilde{t}_r^s$ and $\tilde{N}_{\mathrm{IF}}^{s,j}$ (Zhang et al. 2021); tropospheric slant hydrostatic delay, relativistic effects, tidal loadings, phase wind-up as well as antenna phase center offsets (PCOs) and variations (PCVs) can be corrected by corresponding models (Kouba 2015; Petit and Luzum 2010).

Taking ISBs into account for multi-GNSS kinematic PPP, Eqs. (1) and (2) for multi-GNSS PPP can be expressed as follows:

$$c\delta\tilde{t}_r^s = c\delta\tilde{t}_r^G + ISB_r^s \tag{3}$$

$$\begin{cases} P_{\mathrm{IF}}^{G,j} = \rho_r^{G,j} + c\delta\tilde{t}_r^G + M_r^{G,j} \cdot \mathrm{ZWD}_r + \xi_{\mathrm{IF},r}^{G,j} \\ P_{\mathrm{IF}}^{R,j} = \rho_r^{R,j} + c\delta\tilde{t}_r^G + \mathrm{ISB}_r^R + M_r^{R,j} \cdot \mathrm{ZWD}_r + \xi_{\mathrm{IF},r}^{R,j} \\ P_{\mathrm{IF}}^{E,j} = \rho_r^{E,j} + c\delta\tilde{t}_r^G + \mathrm{ISB}_r^E + M_r^{E,j} \cdot \mathrm{ZWD}_r + \xi_{\mathrm{IF},r}^{E,j} \\ P_{\mathrm{IF}}^{C,j} = \rho_r^{C,j} + c\delta\tilde{t}_r^G + \mathrm{ISB}_r^C + M_r^{C,j} \cdot \mathrm{ZWD}_r + \xi_{\mathrm{IF},r}^{C,j} \end{cases} \tag{4}$$

$$\begin{cases} L_{\mathrm{IF}}^{G,j} = \rho_r^{G,j} + c\delta\tilde{t}_r^G + M_r^{G,j}\cdot \mathrm{ZWD}_r + \tilde{N}_{\mathrm{IF}}^{G,j} + \varepsilon_{\mathrm{IF},r}^{G,j} \\ L_{\mathrm{IF}}^{R,j} = \rho_r^{R,j} + c\delta\tilde{t}_r^G + \mathrm{ISB}_r^R + M_r^{R,j}\cdot \mathrm{ZWD}_r + \tilde{N}_{\mathrm{IF}}^{R,j} + \varepsilon_{\mathrm{IF},r}^{R,j} \\ L_{\mathrm{IF}}^{E,j} = \rho_r^{E,j} + c\delta\tilde{t}_r^G + \mathrm{ISB}_r^E + M_r^{E,j}\cdot \mathrm{ZWD}_r + \tilde{N}_{\mathrm{IF}}^{E,j} + \varepsilon_{\mathrm{IF},r}^{E,j} \\ L_{\mathrm{IF}}^{C,j} = \rho_r^{C,j} + c\delta\tilde{t}_r^G + \mathrm{ISB}_r^C + M_r^{C,j}\cdot \mathrm{ZWD}_r + \tilde{N}_{\mathrm{IF}}^{C,j} + \varepsilon_{\mathrm{IF},r}^{C,j} \end{cases} \tag{5}$$

where ISB_r^s represents the receiver ISB of constellation s. Equation (3) shows that GPS is taken as a reference constellation to estimate ISBs of other GNSS constellations; hence, $\delta\tilde{t}_r^G$ becomes a common parameter in pseudo-range (4) and carrier phase (5) from different constellations.

Stochastic models of ISBs in Kalman filter

In our study, ISB-WN, ISB-RW and ISB-CT are employed to estimate ISBs in multi-GNSS PPP. The stochastic models of the first three strategies are described in this subsection. In addition to those estimation strategies, we also use between-satellite single-difference (SD) observations to eliminate the ISB.

The predicted covariance matrix of states in the Kalman filter can be calculated using

$$\tilde{Q}_i = \Phi_{i-1}\hat{Q}_{i-1}\Phi_{i-1}^T + Q_{W_i} \tag{6}$$

where subscript i and $i-1$ represent the current and last sequential epoch, respectively; $\tilde{Q}_i$ and $\hat{Q}_{i-1}$ denote the predicted and estimated covariance matrix of current and last epoch, respectively; Φ_{i-1} is transform matrix and Q_{W_i} is process noise matrix. The transform coefficient and process noise of ISBs in different strategies are listed in Table 1.

The transform coefficient ϕ_{ISB} and process noise $q_{w,\mathrm{ISB}}$ are the elements in Φ_i and Q_{W_i}, respectively; $q_{0,\mathrm{ISB}}$ denotes the initial ISB variance in $\hat{Q}_0$; τ denotes the time interval between two filter epochs and $\dot{q}_{w,\mathrm{ISB}}$ is the spectral density of ISB, which represents the variation of ISB with time.

Table 1 Transform coefficient and process noise of ISBs with respect to different strategies

Strategy	Transform coefficient ϕ_{ISB}	Process noise $q_{w,ISB}$
ISB-WN	0	$q_{0,ISB}$
ISB-RW	1	$\dot{q}_{w,ISB}\cdot\tau$
ISB-CT	1	0

Equivalence between ISB-WN and ISB-SD

This part contains proof of the mathematical equivalence between estimating ISB with ISB-WN and eliminating ISB with SD observations, termed ISB-SD. The Kalman filter can be written as follows:

$$\hat{X}_i = K_i L_i \tag{7}$$

$$\hat{Q}_i = (I - K_i A_i)\tilde{Q}_i \tag{8}$$

$$K_i = \tilde{Q}_i A_i^T (A_i \tilde{Q}_i A_i^T + P_i^{-1})^{-1} \tag{9}$$

where L_i and P_i^{-1} are the observation vector and the corresponding weight matrix; A_i denotes the geometry matrix; $\hat{X}_i$, $\tilde{Q}_i$ and $\hat{Q}_i$ are unknown vector and the corresponding predicted and estimated covariance matrices; I and K_i are identity and the gain matrix, respectively.

Above Kalman filter is equivalent to the least squares with the constraint of predicted state covariance $\tilde{Q}_i$ at epoch i (Mysen 2017)

$$V_i = \overline{L}_i - \overline{A}_i\hat{X}_i = \begin{bmatrix} L_i \\ 0 \end{bmatrix} - \begin{bmatrix} A_i \\ I \end{bmatrix}\hat{X}_i,\ \overline{P}_i \tag{10}$$

$$\overline{P}_i = \begin{bmatrix} P_i & 0 \\ 0 & \tilde{Q}_i^{-1} \end{bmatrix} \tag{11}$$

$$\hat{X}_i = (A_i^T P_i A_i + \tilde{Q}_i^{-1})^{-1} A_i^T P_i L_i \tag{12}$$

$$\hat{Q}_i = (A_i^T P_i A_i + \tilde{Q}_i^{-1})^{-1} \tag{13}$$

where $\overline{L}_i$ is the new observation vector, V_i denotes residual vector and $\overline{P}_i$ is the new weight matrix containing the constraints for $\hat{X}_i$. Equations (12) and (13) are the equivalent solution of least squares to (7) and (8).

In our study, $\hat{X}_{CLK,i}$ contains δt_r^G and ISBs of the other constellations ISB_r^s of interest. Thus, we take $\hat{X}_{\mathrm{CLK},i}$ from $\hat{X}_i$ and merge the constraint observations of the other parameters with the original observations L_i to get $L_{B,i}$. Then, we obtain the recombined least squares format equation of (10):

$$V_i = \begin{bmatrix} L_{B,i} \\ 0_{n\times 1} \end{bmatrix} - \begin{bmatrix} A_{B_{\mathrm{PAR}},i} & A_{B_{\mathrm{CLK}},i} \\ 0_{n\times z} & I_{n\times n} \end{bmatrix} \begin{bmatrix} \hat{X}_{\mathrm{PAR},i} \\ \hat{X}_{\mathrm{CLK},i} \end{bmatrix},\ \begin{bmatrix} P_{B,i} & C_{\mathrm{PQ},i} \\ C_{\mathrm{PQ},i}^T & \tilde{Q}_{\mathrm{CLK},i}^{-1} \end{bmatrix} \tag{14}$$

$$L_{B,i} = \begin{bmatrix} L_i \\ 0_{z\times 1} \end{bmatrix},\ P_{B,i} = \begin{bmatrix} P_i & 0 \\ 0 & \tilde{Q}_{\mathrm{PAR},i}^{-1} \end{bmatrix} \tag{15}$$

$$A_{B_{\mathrm{PAR}},i} = \begin{bmatrix} A_{\mathrm{PAR},i} \\ I_{z\times z} \end{bmatrix},\ A_{B_{\mathrm{CLK}},i} = \begin{bmatrix} A_{\mathrm{CLK},i} \\ 0_{z\times n} \end{bmatrix} \tag{16}$$

where the subscript CLK represents n receiver clock-related parameters (δt_r^G and ISB_r^s), PAR represents the other z parameters (receiver coordinates, ZWD_r and $\tilde{N}_{\mathrm{IF}}^{s,i}$) and B represents the combination between original and constraint observations.

Note that the correlation matrix $C_{\mathrm{PQ},i}$ expresses the covariance between PAR and CLK in $\tilde{Q}_i$. However, the ISB-WN strategy eliminates the covariance, then (14) becomes

$$V_i = \begin{bmatrix} L_{B,i} \\ 0_{n\times 1} \end{bmatrix} - \begin{bmatrix} A_{B_{\mathrm{PAR}},i} & A_{B_{\mathrm{CLK}},i} \\ 0_{n\times z} & I_{n\times n} \end{bmatrix} \begin{bmatrix} \hat{X}_{\mathrm{PAR},i} \\ \hat{X}_{\mathrm{CLK},i} \end{bmatrix}, \begin{bmatrix} P_{B,i} & 0 \\ 0 & \tilde{Q}^{-1}_{\mathrm{CLK},i} \end{bmatrix} \tag{17}$$

where $C_{PQ,i}$ is zero.

The *CLK* parameters can be eliminated by SD observations between satellites. The equivalent least squares format equation to Kalman filter of ISB-SD strategy is

$$V_{\mathrm{SD},i} = \begin{bmatrix} L_{\mathrm{SD},i} \\ 0 \end{bmatrix} - \begin{bmatrix} A_{\mathrm{SD}_{\mathrm{PAR}},i} \\ I \end{bmatrix} \hat{X}_{\mathrm{PAR},i}, \begin{bmatrix} P_{\mathrm{SD},i} & 0 \\ 0 & \tilde{Q}^{-1}_{\mathrm{PAR},i} \end{bmatrix} \tag{18}$$

$$L_{\mathrm{SD},i} = D_i \cdot L_i,\ A_{\mathrm{SD}_{\mathrm{PAR}},i} = D_i \cdot A_{\mathrm{PAR},i},\ P_{\mathrm{SD},i} = D_i \cdot P_i \tag{19}$$

where D_i is the transformation matrix from undifferenced observations to the SD one:

$$D_i = \begin{bmatrix} D_i^G & & & \\ & D_i^R & & \\ & & D_i^E & \\ & & & D_i^C \end{bmatrix} \tag{20}$$

$$D_i^s = \begin{bmatrix} -1 & & 1 & & \\ & \ddots & \vdots & & \\ & & -1 & 1 & \\ & & & 1 & -1 \\ & & & \vdots & & \ddots \\ & & & 1 & & & -1 \end{bmatrix}_{(n^s-1)\times n^s} \tag{21}$$

where n^s and D_i^s denote the satellite number and SD transformation matrix of constellation s based on the selected reference satellite.

Now we prove the equivalence between (17) and (18). The least squares solution of (17) is

$$\hat{X}_i = (A_{\mathrm{PT},i}^T P_{B,i} A_{\mathrm{PT},i} + \tilde{Q}^{-1}_{\mathrm{CLK},i})^{-1} A_{\mathrm{PT},i}^T P_{B,i} L_{B,i} \tag{22}$$

$$\hat{Q}_i = (A_{\mathrm{PT},i}^T P_{B,i} A_{\mathrm{PT},i} + \tilde{Q}^{-1}_{\mathrm{CLK},i})^{-1} \tag{23}$$

$$A_{PT,i} = \begin{bmatrix} A_{B_{PAR},i} & A_{B_{CLK},i} \end{bmatrix} \tag{24}$$

where $\tilde{Q}^{-1}_{CLK,i}$ is negligible enough to be eliminated from (22) and (23), as the noise of *CLK* parameters is usually large when applying ISB-WN to δt_r^G and ISB_r^s. Then, (22) and (23) become

$$\hat{X}_i = (A_{\mathrm{PT},i}^T P_{B,i} A_{\mathrm{PT},i})^{-1} A_{\mathrm{PT},i}^T P_{B,i} L_{B,i} \tag{25}$$

$$\hat{Q}_i = (A_{\mathrm{PT},i}^T P_{B,i} A_{\mathrm{PT},i})^{-1} \tag{26}$$

which is the solution of the residual equation

$$V_i = L_{B,i} - \begin{bmatrix} A_{B_{\mathrm{PAR}},i} & A_{B_{\mathrm{CLK}},i} \end{bmatrix} \begin{bmatrix} \hat{X}_{\mathrm{PAR},i} \\ \hat{X}_{\mathrm{CLK},i} \end{bmatrix}, P_{B,i} \tag{27}$$

where the constraints of δt_r^G and ISB_r^s are removed in comparison with (17). According to (15) and (16), (27) can be written as follows:

$$V_i = \begin{bmatrix} L_i \\ 0 \end{bmatrix} - \begin{bmatrix} A_{\mathrm{PAR},i} & A_{\mathrm{CLK},i} \\ I & 0 \end{bmatrix} \begin{bmatrix} \hat{X}_{\mathrm{PAR},i} \\ \hat{X}_{\mathrm{CLK},i} \end{bmatrix}, \begin{bmatrix} P_i & 0 \\ 0 & \tilde{Q}^{-1}_{\mathrm{PAR},i} \end{bmatrix} \tag{28}$$

where we can eliminate the parameters $\hat{X}_{\mathrm{CLK},i}$ from (28) according to (19) and keep the equivalence at the same time (Schaffrin and Grafarend 1986; Xu and Xu 2016). Then, we obtain

$$V_{SD,i} = \begin{bmatrix} L_{SD,i} \\ 0 \end{bmatrix} - \begin{bmatrix} A_{SD_{\mathrm{PAR}},i} \\ I \end{bmatrix} \hat{X}_{\mathrm{PAR},i}, \begin{bmatrix} P_{\mathrm{SD},i} & 0 \\ 0 & \tilde{Q}^{-1}_{\mathrm{PAR},i} \end{bmatrix} \tag{29}$$

which is the same as (18).

The present demonstration provides the equivalence between ISB-WN and ISB-SD strategies. It is recalled that this demonstration requires that the covariance $C_{\mathrm{PQ},i}$ between PAR and CLK is zero, and the predicted covariance $\tilde{Q}_{\mathrm{CLK}}$ of δt_r^G and ISB_r^s is large, which is in accordance with the ISB-WN strategy.

Data processing setup

To evaluate the performance of the four aforementioned ISB estimation strategies in multi-GNSS kinematic PPP, both static and kinematic tests were conducted, with the precise orbit and 30-s sampling clock products provided by CODE, GFZ and WHU. In multi-GNSS PPP, observations from GPS, GLONASS, Galileo and BDS were processed together. For BDS, both inclined geosynchronous orbit (IGSO) and medium earth orbit (MEO) satellites of BDS-2 and BDS-3 satellites were involved, except geosynchronous earth orbit (GEO). The reason is that those GEOs are not included by CODE in the final MGEX precise products (Guo et al. 2016; Montenbruck et al. 2017; Prange et al. 2017), and comparability among the products from different ACs has been guaranteed.

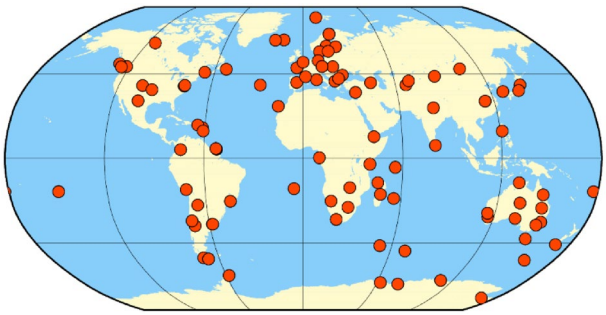

Fig. 1 Global distribution of selected 112 MGEX stations

Fig. 2 Urban trajectory (yellow) and base station (blue) of vehicular test in Weihai, China

Experimental data

In the static test, 30-s sampled observations at 112 permanent stations from the MGEX network were selected, which covered the day of year (DOY) from 210 to 230 in 2021. The global distribution of these stations is shown in Fig. 1. All selected stations track GPS, GLONASS, Galileo and BDS-2/3 satellites.

A vehicular test was conducted to assess the performance of kinematic multi-GNSS PPP in real dynamic applications using different ISB solution strategies. Figure 2 shows the two-hour vehicular trajectory in the city of Weihai, China. A NovAtel PwrPak7-E2 receiver was used to collect one-Hertz multi-GNSS observations of the vehicle. Moreover, a base station was set up at Shandong University in Weihai, equipped with a Septentrio PolaRx5 receiver. Its precise coordinates were known beforehand to implement double-difference (D.D.) relative positioning and produce the reference trajectory for the multi-GNSS kinematic PPP solution.

Processing strategy

In the GNSS analysis, the tropospheric ZWD was estimated as a random walk process with a spectral density $\dot{q}_{w,\mathrm{ZWD}}$ of 10^{-8} m^2/s. The IF ambiguities were estimated as float constants in each continuously observed arc. For kinematic positioning, white noise of 30^2 m^2 was applied for each component of coordinate parameters. Cycle slips were detected by Loss of Lock Indicator (LLI), Hatch–Melbourne–Wubbena and geometry-free combinations (Sanz et al. 2013; Leick et al. 2015). Once a cycle slip is detected, the corresponding ambiguity is reset to an initial value of the difference between pseudo-range and carrier phase, with an initial noise of 10^2 m^2. In the Kalman filter, the initial variance of ISB, as well as the process noise for ISB-WN, was set to 60^2 m^2, while the spectral density $\dot{q}_{w,\mathrm{ISB}}$ for ISB-RW was set to 10^{-6} m^2/s (Li and Zhang 2014; Zhou et al. 2019).

The elevation cutoff angle was set to 15°, and an elevation-dependent weighting method of $\sin^{-2}$(elevation) for both pseudo-ranges and carrier phases was applied. The 90° elevation noise levels of the carrier phase were set to 0.003 m. The noise ratio between pseudo-range and phase measurements was set to 100 for the MGEX stations, while that for the vehicular observations was adjusted to 300, to consider larger multipath errors in the urban case (Dixon 1991; Meguro et al. 2009; Sokhandan et al. 2016).

The PPP performance in terms of convergence time, positioning accuracy and differences of ISB estimates was analyzed to assess the ISB solution strategies. For MGEX stations in static and pseudo-kinematic test, we adopted the convergence condition defined as the first epoch when the positioning error in each component of east (E), north (N) and up (U) is smaller than 0.1 m, as well as in the following 20 epochs (Jiang et al. 2017). At 30-s sampling interval, the convergence criterion corresponds to 10 min. The daily root-mean-square (RMS), with respect to the coordinates provided by IGS weekly solutions, was calculated after convergence to assess the positioning accuracy. In the kinematic test, we kept the convergence threshold of E and N as 0.1 m and increased the threshold of U to 0.2 m, since the positioning performance is degraded with real dynamic data (Cai and Gao 2013). Furthermore, the convergence instant was determined only when the positioning errors from the current epoch to the final were all under the convergence threshold in each component, and the positioning RMS was calculated based on the kinematic PPP solution during the whole dynamic test period except the first 30 min. Finally, to compare the ISB solutions obtained with different strategies, the mean values and standard deviations (STDs) of ISB differences of ISB-CT vs. ISB-RW, ISB-CT vs. ISB-WN and ISB-RW vs. ISB-WN were calculated.

ISB strategies performance in static test

In order to verify that GFZ currently adopts the analogous ISB strategy as CODE and WHU in satellite clock estimation, we first present the statistics of ISB solutions with static data. The 1-day ISB series of station WUH2 derived from kinematic PPP solutions based on different strategies are shown as an example in Fig. 3. In order to improve the comparison, the ISB obtained by ISB-CT of the last epoch is removed as the datum in each panel of the figure. Same as with CODE and WHU products, the ISB series of the three constellations agree well among the different strategies with GFZ products. Table 2 lists the mean values and STDs of ISB differences between three pairs of strategies for comparison. It shows that the ISB differences for strategies with GFZ products differ from that with CODE and WHU products by less than 0.05 ns, which confirms that the consistent ISB strategies are applied by CODE, GFZ and WHU in satellite clock estimation. Generally, the mean values and STDs of ISB difference are less than 0.05 ns and 0.1 ns, respectively. Furthermore, the ISB differences of ISB-RW vs. ISB-WN are almost zero, which indicates that ISB-RW and ISB-WN strategies are more consistent than ISB-CT in ISB estimation.

Taking station WUH2 as an example, Fig. 4 shows the positioning errors among four ISB estimation strategies on DOY 210, 2021. The left panel shows that the positioning error series of ISB-WN solution is coincident with that of ISB-SD in all components. In the right panel, ISB-RW and ISB-CT strategies show slightly different in positioning errors. The aggregated RMSs of all stations with respect to four ISB strategies and different precise products during the test period are presented in Table 3. Generally, the positioning accuracy with three precise products is comparable, and the horizontal and vertical components are better than 1.5 and 3.0 cm, respectively. The positioning accuracy among four ISB strategies shows no significant difference, which indicates that applying different ISB strategies hardly affects the positioning accuracy of multi-GNSS kinematic PPP at permanent stations.

Figure 5 shows the distribution and statistics of daily convergence time over all MGEX stations from DOY 210 to 213, 2021, to assess the convergence performance of multi-GNSS kinematic PPP based on different ISB strategies. Generally, the positioning errors of more than 80% of test cases converge into 0.1 m within 40 min when using different ISB strategies with CODE, GFZ and WHU precise products. The histogram shows that convergence time distributions and statistical results are almost the same among ISB-WN, ISB-SD and ISB-RW strategies. The ISB-CT strategy accounts for

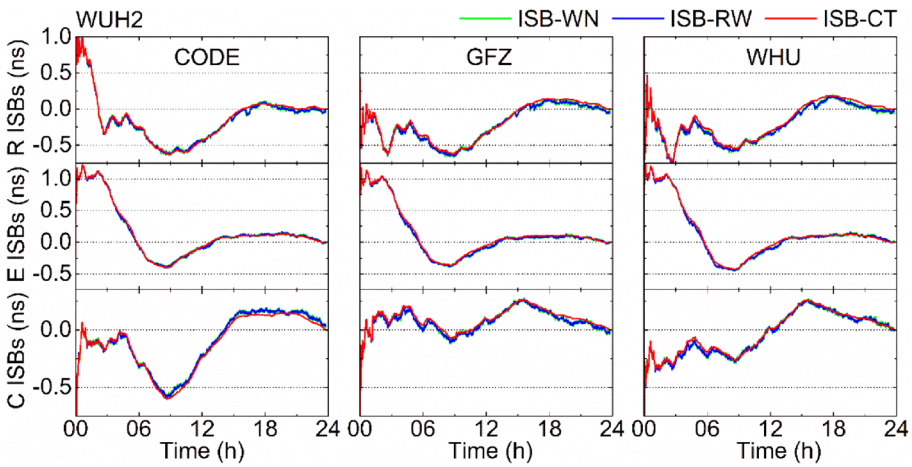

Fig. 3 GLONASS (R, top row), Galileo (E, middle row) and BDS (C, bottom row) ISB series of station WUH2 produced by ISB-WN (green), ISB-RW (blue) and ISB-CT (red) strategies with CODE (left column), GFZ (central column) and WHU (right column) products on DOY 210, 2021

Table 2 Mean values and STDs (in parentheses) of GLONASS, Galileo and BDS ISB differences for ISB-CT, ISB-RW and ISB-WN strategies in the static test

Compared strategies	CODE			GFZ			WHU		
	R	E	C	R	E	C	R	E	C
CT versus RW	−0.03 (0.04)	−0.01 (0.02)	−0.01 (0.03)	−0.02 (0.05)	−0.01 (0.03)	−0.00 (0.07)	−0.03 (0.05)	0.00 (0.03)	−0.00 (0.04)
CT versus WN	−0.03 (0.05)	−0.00 (0.02)	−0.01 (0.03)	−0.01 (0.05)	−0.01 (0.03)	−0.00 (0.07)	−0.03 (0.06)	0.00 (0.03)	−0.00 (0.04)
RW versus WN	−0.00 (0.02)	−0.00 (0.01)	−0.00 (0.01)	−0.00 (0.02)	−0.00 (0.02)	−0.00 (0.03)	−0.00 (0.02)	−0.00 (0.02)	−0.00 (0.02)

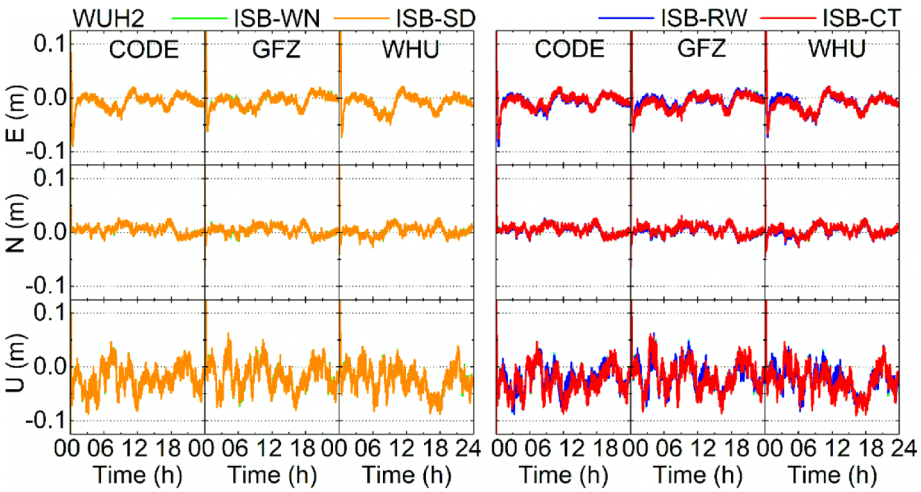

Fig. 4 Time series of kinematic PPP errors of station WUH2 with CODE, GFZ and WHU products using ISB-WN and ISB-SD (left) and ISB-RW and ISB-CT (right) strategies on DOY 210, 2021

Table 3 Positioning RMSs (cm) of multi-GNSS kinematic PPP for MGEX stations based on different ISB strategies and precise products

Strategy	CODE			GFZ			WHU		
	E	N	U	E	N	U	E	N	U
ISB-WN	1.2	0.9	2.8	1.4	1.0	3.0	1.2	1.0	2.7
ISB-SD	1.2	0.9	2.8	1.4	1.0	3.0	1.2	1.0	2.7
ISB-RW	1.2	0.9	2.7	1.4	1.0	3.0	1.2	1.0	2.7
ISB-CT	1.1	0.8	2.7	1.3	1.0	3.0	1.2	1.0	2.7

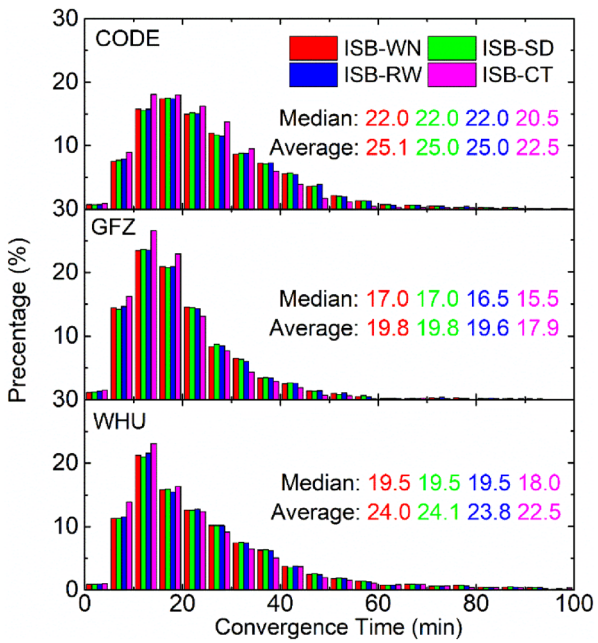

Fig. 5 Distribution and statistics of daily convergence time over all MGEX stations in multi-GNSS kinematic PPP with different precise products CODE (top), GFZ(middle) and WHU (bottom), where the listed medians and averages are in the order of ISB-WN, ISB-SD, ISB-RW and ISB-CT

a larger proportion of the cases with a shorter convergence time rather than the other three strategies: In the results with CODE precise products, the percentage employing ISB-CT strategy is about 8% higher than using other strategies in the convergence time under 35 min; with GFZ products, the ISB-CT solution presents a higher percentage in the convergence time within 20 min, which is about 7% higher than solutions of the other three strategies; and with WHU products, the ISB-CT strategy produces about 5% more cases with a convergence time under 20 min. Combining the statistical results of three precise products, the ISB-CT strategy reduces the average and median convergence time by 1.5 and 2.0 min, respectively.

ISB strategies performance in kinematic test

In this section, the performances of ISB estimation strategies in multi-GNSS kinematic PPP are analyzed and evaluated with respect to the vehicular test first, and the results of a pseudo-kinematic test are presented to further verify our findings.

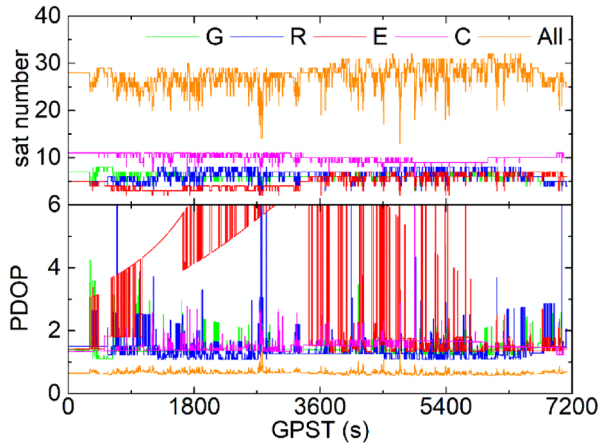

Fig. 6 Satellite number and PDOP during the vehicular test period

Vehicular kinematic test result

The number of available satellites and positioning dilution of precision (PDOP) during the period of the vehicular test in the urban case is shown in Fig. 6. As it can be seen, the average satellite numbers for GPS, GLONASS or Galileo are fewer than 10 except for BDS, as the regional IGSO satellites are involved in this test. The PDOP of every constellation is higher than 1.0 during the experimental period. A better positioning condition is achieved by combining the four constellations: The average satellite number and PDOP are 27 and 0.7, respectively. Blocked by the high constructions along the trajectory, the tracking of satellite signals varies during the test period, but the kinematic PPP is still achieved in every epoch with at least 13 available satellites observed and a maximum PDOP of 1.7 in the multi-GNSS processing.

The ISB estimates based on ISB-WN, ISB-RW and ISB-CT strategies are also analyzed for the kinematic test. Figure 7 shows the ISB series of different constellations based on the three ISB strategies, where the ISB obtained by ISB-CT of the last epoch is removed as the datum in each panel. The jump of the Galileo ISB at 5386 s for ISB-WN is caused by the loss of all six available Galileo satellite tracking. Identical to the static test, the ISB derived from ISB-WN, ISB-RW and ISB-CT solutions have almost the same varying trend in the kinematic test, no matter what precise products are used. The statistics of ISB differences among the three ISB strategies are presented in Table 4, where the mean values and STDs of Galileo are calculated with the ISB series before the loss of tracking. Same as in the static test, the ISB differences based on GFZ products highly agree with that based on CODE and WHU products, which further confirms the consistency of their satellite clock products. The mean values and STDs of ISB differences among

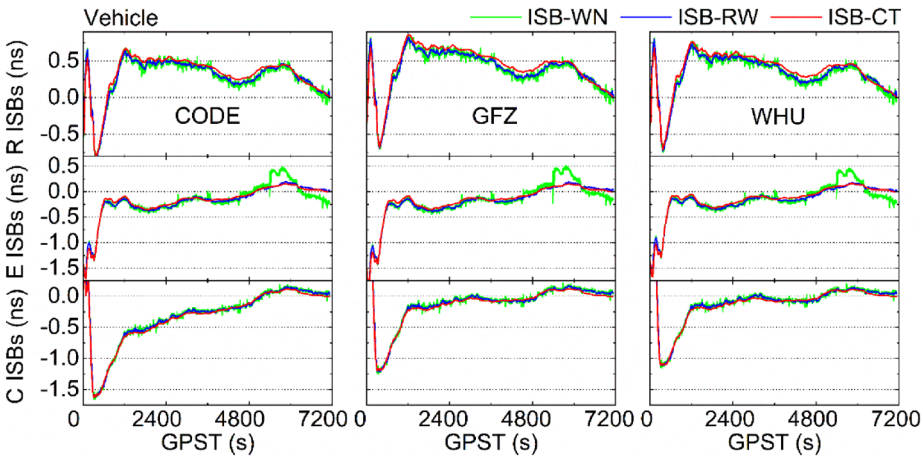

Fig. 7 GLONASS, Galileo and BDS ISB series of ISB-WN, ISB-RW and ISB-CT solutions based on CODE, GFZ and WHU products in vehicular test

Table 4 Mean values and STDs (in parentheses) of GLONASS, Galileo and BDS ISBs differences among ISB-CT, ISB-RW and ISB-WN strategies in vehicular test

Compared strategies	CODE			GFZ			WHU		
	R	E	C	R	E	C	R	E	C
CT versus RW	−0.05 (0.02)	−0.03 (0.02)	0.01 (0.02)	−0.07 (0.02)	−0.03 (0.02)	0.01 (0.02)	−0.06 (0.02)	−0.04 (0.02)	0.01 (0.03)
CT versus WN	−0.05 (0.03)	−0.02 (0.05)	0.01 (0.03)	−0.07 (0.03)	−0.03 (0.05)	0.01 (0.03)	−0.06 (0.04)	−0.03 (0.05)	0.01 (0.03)
RW versus WN	−0.01 (0.02)	0.00 (0.03)	0.00 (0.01)	−0.01 (0.02)	0.00 (0.03)	0.00 (0.01)	−0.01 (0.02)	0.00 (0.03)	0.00 (0.01)

different strategies are less than 0.1 ns. Moreover, the ISBs estimated by ISB-RW and ISB-WN are closer to each other than by ISB-CT, which imply the different positioning performance based on ISB-CT strategy from ISB-RW and ISB-WN in the vehicular test.

The positioning errors of vehicular test in time series with respect to different ISB strategies are shown in Fig. 8. Generally, the kinematic PPP with different precise products presents comparable positioning performance. After the convergence, the positioning errors in all cases are stable within 0.1 m and 0.2 m in the horizontal and vertical components, respectively. The left panel shows that the positioning error series of ISB-WN solutions are almost coincident with that of ISB-SD. A distinct difference between ISB-CT and ISB-RW solutions can be seen in the right panel. Specifically, the convergence time of ISB-CT solution is 10.3 and 11.8 min shorter than that of ISB-RW solution in the E and N component, by averaging the results based on CODE, GFZ and WHU products. In the U component, the positioning errors of ISB-RW solutions vary around 0.2 m in the first hour of the test, while ISB-CT solutions only take a few minutes to converge to the threshold.

Figure 8 shows the positioning errors based on ISB-WN, ISB-SD and ISB-RW in E and N converged into the corresponding threshold before those in U. Thus, the convergence times of these three strategies are all determined by the U component. For the ISB-CT solution, the figure illustrates that the convergence time depends on the E and N components, as errors in the U component converge into 0.2 m only several minutes after positioning. The statistical results of convergence time with respect to different ISB strategies are presented in Table 5. Similar to the positioning errors, the performance of convergence time is close among the solutions based on CODE, GFZ and WHU products, and the ISB-SD strategy performs as well as ISB-WN in convergence time. Furthermore, the average convergence time obtained by the ISB-CT strategy is 23.5 min, which improves the performance by 60.1% in comparison with the 59.6 min obtained by the other three strategies.

The positioning accuracy of the vehicular test is assessed and compared among ISB strategies according to the RMSs with respect to the D.D. positioning result. Table 6 shows the positioning RMSs with different precise products in each component. Generally, the positioning accuracy in two horizontal components is comparable among the solution with CODE, GFZ and WHU products, as the difference is less than 5.0 mm. In the vertical component, the RMS error with

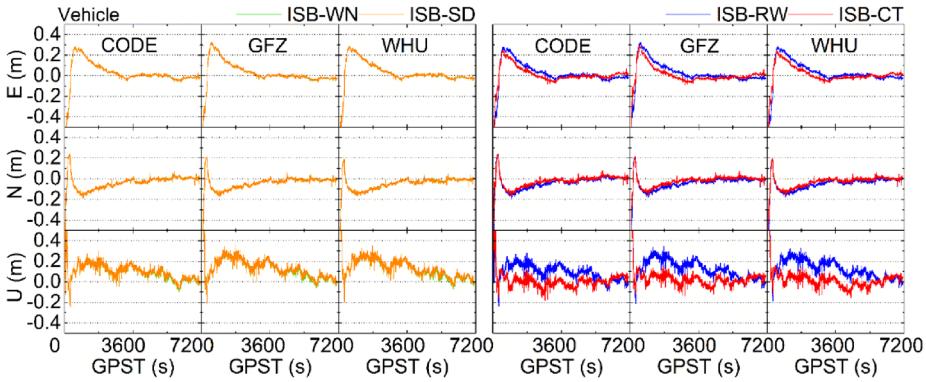

Fig. 8 Time series of kinematic PPP errors of ISB-WN and ISB-SD (left) and ISB-RW and ISB-CT (right) solutions with CODE, GFZ and WHU products in vehicular test

Table 5 Convergence time (minutes) of kinematic PPP based on different ISB strategies in vehicular test

AC	ISB-WN	ISB-SD	ISB-RW	ISB-CT
CODE	58.7	58.7	58.8	23.7
GFZ	60.1	60.1	61.5	22.7
WHU	60.0	60.0	59.9	24.0

Table 6 Positioning RMSs (cm) of vehicular test with respect to different ISB strategies and precise products

Strategy	CODE			GFZ			WHU		
	E	N	U	E	N	U	E	N	U
ISB-WN	2.9	3.7	10.0	3.1	3.6	13.1	3.2	4.0	12.8
ISB-SD	2.9	3.7	10.1	3.0	3.6	13.3	3.2	4.0	13.0
ISB-RW	2.8	3.7	9.9	2.9	3.6	13.2	3.1	4.0	12.7
ISB-CT	2.4	2.5	4.2	2.7	2.0	4.3	2.5	2.4	4.6

CODE products is about 3.0 cm lower than the solutions with GFZ or WHU products when ISB-WN, ISB-SD and ISB-RW strategies are employed. In ISB-CT solutions, the RMS error is comparable with different precise products, and the average accuracy of 2.5, 2.3 and 4.4 cm in the E, N and U components is achieved. Compared to the other three strategies, the ISB-CT improves the positioning accuracy by 16.3% and 32.4% in the E and N with CODE products, 9.9% and 44.4% with GFZ products as well as 21.0% and 40.0% with WHU products. The greatest improvement is achieved in the U component using the ISB-CT strategy, with 58.0%, 67.4% and 64.2% with CODE, GFZ and WHU products, respectively.

Pseudo-kinematic test result

Compared with permanent MGEX stations, the dynamic receiver in the urban case tracks fewer satellites and experiences more frequent cycle slips, which makes the satellite set vary. Numerically, the number of estimated ambiguities in the filter is 2431/hour for the vehicular receiver, but that for permanent stations is only 30/hour on average. Therefore, the ISB-CT strategy contributes more to the estimation of the coordinates with its inherent robust feature for the dynamic data.

To further verify if the ISB-CT strategy benefits multi-GNSS data with more cycle slips, we artificially increased the number of cycle slips of permanent MGEX stations to reach the same level as the vehicular data for pseudo-kinematic test. It should be noted that the previous figure of 2431 estimated ambiguities per hour is counted from one-Hertz vehicular data, taking into account multiple cycle slips of each satellite within every 30 s. Those duplicated cycle slips are counted as one to meet the sampling of permanent stations; hence, the number of estimated ambiguities is set as 880/hour in this test. Moreover, only CODE products are employed in this part, as the two previous tests have verified that the different products have the same performance under the same ISB strategy.

The positioning errors in time series of the same example WUH2 on DOY 210, 2021, are shown in Fig. 9. Compared with the static test, the positioning errors of ISB-WN and ISB-SD are still almost the same, but that of ISB-CT show more difference from the other three strategies. Table 7 shows the statistics of positioning RMSs and convergence time during the test period. Same as the static and kinematic test, the ISB-WN and ISB-SD perform the same as each other with pseudo-kinematic data. Compared with ISB-WN, ISB-SD and ISB-RW, ISB-CT improves the positioning accuracy by 21.2%, 19.6% and 16.8% on E, N and U component, respectively. The median and average convergence times obtained by ISB-CT are 24.0% and 24.7% shorter than that of the other strategies. Considering the similar

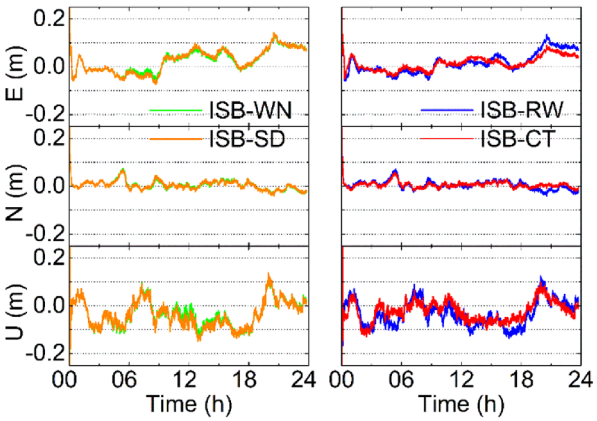

Fig. 9 Time series of pseudo-kinematic PPP errors of station WUH2 with CODE products using ISB-WN and ISB-SD (left) and ISB-RW and ISB-CT (right) strategies on DOY 210, 2021

Table 7 Positioning RMSs and convergence time of pseudo-kinematic test based on different ISB strategies with CODE products

Strategy	Positioning RMSs (cm)			Convergence time (minutes)	
	E	N	U	Median	Average
ISB-WN	5.3	3.1	6.2	43.5	54.4
ISB-SD	5.2	3.1	6.2	43.5	54.4
ISB-RW	5.1	3.0	6.0	41.5	52.5
ISB-CT	4.1	2.5	5.1	32.5	40.4

performance of ISB-CT and the other strategies in the static test, this test verifies that ISB-CT can improve the positioning performance for the data with more cycle slips.

Conclusions

The present study evaluated the performance of different strategies to estimate ISB in the multi-GNSS kinematic PPP: ISB-WN, ISB-RW, ISB-CT and ISB-SD. The equivalence between ISB-WN and ISB-SD strategy in multi-GNSS PPP was demonstrated. To assess the four ISB strategies, static, real and pseudo-kinematic tests based on 1-month MGEX stations and urban vehicular data were conducted with CODE, GFZ and WHU precise products.

We conclude that the four strategies produce comparable ISB estimates and positioning accuracy in the static test, but the ISB-CT strategy can slightly shorten convergence time. In the real and pseudo-kinematic tests with more cycle slips and estimated ambiguities in the filter, the ISB-CT strategy can improve positioning accuracy and reduce the convergence time. The equivalence between ISB-WN and ISB-SD is confirmed in both static and

kinematic tests. The difference in ISB estimates proves that the current satellite clock products of GFZ are consistent with that of CODE and WHU since GFZ has been applying the 1-day constant model for ISB from 2019 onwards.

Acknowledgements The study is funded by Laoshan Laboratory (LSKJ202205104, LSKJ202205104_01), National Key Research and Development Program of China (2020YFB0505800, 2020YFB0505804), National Natural Science Foundation of China (42004012), Natural Science Foundation of Shandong Province, China (ZR2020QD048) and by the project RTI2018-094295-B-I00 funded by the MCIN/AEI 1013039/501100011033 which is co-funded by the FEDER program.

Data availability The MGEX station observations, multi-GNSS precise orbit and clock products can be achieved at https://cddis.nasa.gov/archive/gnss/. The other datasets employed in this study are available from the corresponding author.

References

De Bakker PF, Tiberius CCJM (2017) Real-time multi-GNSS single-frequency precise point positioning. GPS Solut 21(4):1791–1803. https://doi.org/10.1007/s10291-017-0653-2

Cai C, Gao Y (2013) Modeling and assessment of combined GPS/GLONASS precise point positioning. GPS Solut 17(2):223–236. https://doi.org/10.1007/s10291-012-0273-9

Dixon TH (1991) An introduction to the global positioning system and some geological applications. Rev Geophys 29(2):249–276. https://doi.org/10.1029/91rg00152

Gao W, Meng X, Gao C, Pan S, Wang D (2018) Combined GPS and BDS for single-frequency continuous RTK positioning through real-time estimation of differential inter-system biases. GPS Solut 22(1):1–13. https://doi.org/10.1007/s10291-017-0687-5

Guo J, Xu X, Zhao Q, Liu J (2016) Precise orbit determination for quad-constellation satellites at Wuhan University: strategy, result validation, and comparison. J Geod 90(2):143–159. https://doi.org/10.1007/s00190-015-0862-9

Hong J, Tu R, Gao Y, Zhang R, Fan L, Zhang P, Liu J (2019) Characteristics of inter-system biases in Multi-GNSS with precise point positioning. Adv Space Res 63(12):3777–3794. https://doi.org/10.1016/j.asr.2019.02.037

Jiang N, Xu Y, Xu T, Xu G, Sun Z, Schuh H (2017) GPS/BDS short-term ISB modelling and prediction. GPS Solut 21(1):163–175. https://doi.org/10.1007/s10291-015-0513-x

Jiang N, Xu T, Xu Y, Xu G, Schuh H (2019) Assessment of different stochastic models for inter-system bias between GPS and BDS. Remote Sens. https://doi.org/10.3390/rs11080989

Kouba J (2015) A guide to using international GNSS service (IGS) products. In. https://kb.igs.org/hc/en-us/articles/201271873-A-Guide-to-Using-the-IGS-Products. Accessed 11 January 2022

Leick A, Rapoport L, Tatarnikov D (2015) GPS satellite surveying. John Wiley & Sons

Li P, Zhang X (2014) Integrating GPS and GLONASS to accelerate convergence and initialization times of precise point positioning. GPS Solut 18(3):461–471. https://doi.org/10.1007/s10291-013-0345-5

Li X, Zhang X, Ren X, Fritsche M, Wickert J, Schuh H (2015) Precise positioning with current multi-constellation global navigation satellite systems: GPS, GLONASS Galileo and BeiDou. Sci Rep 5(1):1–14. https://doi.org/10.1038/srep08328

Liu T, Yuan Y, Zhang B, Wang N, Tan B, Chen Y (2017) Multi-GNSS precise point positioning (MGPPP) using raw observations. J Geod 91(3):253–268. https://doi.org/10.1007/s00190-016-0960-3

Liu X, Jiang W, Chen H, Zhao W, Huo L, Huang L, Chen Q (2019) An analysis of inter-system biases in BDS/GPS precise point positioning. GPS Solut 23(4):1–14. https://doi.org/10.1007/s10291-019-0906-3

Meguro JI, Murata T, Takiguchi JI, Amano Y, Hashizurne T (2009) GPS multipath mitigation for urban area using omnidirectional infrared camera. IEEE Trans Intell Transp Syst 10(1):22–30. https://doi.org/10.1109/tits.2008.2011688

Montenbruck O et al (2017) The multi-GNSS experiment (MGEX) of the international GNSS service (IGS) - achievements, prospects and challenges. Adv Space Res 59(7):1671–1697. https://doi.org/10.1016/j.asr.2017.01.011

Mysen E (2017) On the equivalence of Kalman filtering and least-squares estimation. J Geod 91(1):41–52. https://doi.org/10.1007/s00190-016-0936-3

Paziewski J, Wielgosz P (2015) Accounting for Galileo-GPS inter-system biases in precise satellite positioning. J Geod 89(1):81–93. https://doi.org/10.1007/s00190-014-0763-3

Petit G, Luzum B (2010) IERS conventions (2010). In: IERS Technical Note No. 36. Verlag des Bundesamts für Kartographie und Geodäsie, Frankfurt am Main. http://www.iers.org/TN36/

Prange L, Orliac E, Dach R, Arnold D, Beutler G, Schaer S, Jaggi A (2017) CODE's five-system orbit and clock solution-the challenges of multi-GNSS data analysis. J Geod 91(4):345–360. https://doi.org/10.1007/s00190-016-0968-8

Sanz J, Juan JM, Hernández-Pajares M (2013) GNSS data processing. In: Fletcher K (ed) Fundamentals and algorithms, vol I. ESA Communications, Noordwijk

Schaffrin B, Grafarend E (1986) Generating classes of equivalent linear models by nuisance parameter. Manuscr Geod 11:262–271

Sokhandan N, Curran JT, Broumandan A, Lachapelle G (2016) An advanced GNSS code multipath detection and estimation algorithm. GPS Solut 20(4):627–640. https://doi.org/10.1007/s10291-015-0475-z

Tian Y, Liu Z, Ge M, Neitzel F (2018) Determining inter-system bias of GNSS signals with narrowly spaced frequencies for GNSS positioning. J Geod 92(8):873–887. https://doi.org/10.1007/s00190-017-1100-4

Xu G, Xu Y (2016) GPS observation equations and equivalence properties. GPS: theory, algorithms and applications, 3rd edn. Springer, Berlin Heidelberg, Berlin, Heidelberg, pp 133–185. https://doi.org/10.1007/978-3-662-50367-6_6

Zhang B, Hou P, Zha J, Liu T (2021) Integer-estimable FDMA model as an enabler of GLONASS PPP-RTK. J Geod 91:1–21. https://doi.org/10.1007/s00190-021-01546-0

Zhou F, Dong D, Li P, Li X, Schuh H (2019) Influence of stochastic modeling for inter-system biases on multi-GNSS undifferenced and uncombined precise point positioning. GPS Solut 23(3):1–13. https://doi.org/10.1007/s10291-019-0852-0

Mowen Li received his master's degree at Shandong University in 2019 and is a Ph.D. candidate of Shandong University and Universitat Politecnica de Catalunya. His current research focuses on the resilient integration technology of GNSS, INS and other sensors.

Adria Rovira-Garcia is a Serra Hunter Fellow with the Department of Physics (UPC) and a member of gAGE since 2009. He co-authors 29 papers in peer-reviewed journals, two book chapters and over 50 works in meeting proceedings, with one best presentation award from the US Institute of Navigation. His research interests are focused on high-accuracy navigation under scintillation.

Wenfeng Nie obtained his BSc and MSc degrees in 2012 and 2014 from Southeast University and a Ph.D. degree in theoretical physics from Shandong University, China, in 2019. He is currently a Research Associate with the Institute of Space Science at Shandong University, China. His current research activities are related to ionospheric Remote Sensing and precise GNSS data processing.

Tianhe Xu is a professor at the Institute of Space Sciences at Shandong University, Weihai. He received his Ph.D. and M.S. degrees in Geodesy from the Zhengzhou Institute of Surveying and Mapping of China in 2004 and 2001. He worked in the GFZ as a visiting scientist from 2009 to 2011. His research interests are satellite navigation, resilient integration of multi-sensors, orbit determination, satellite gravity data processing and quality control.

Guochang Xu obtained his Ph.D. from the Technical University Berlin in 1992. Having worked as a scientist at the GFZ from 1993 to 1998 and as a senior scientist at the National Survey and Cadastre, Denmark, from 1998 to 1999, he returned to GFZ as a senior scientist in 1999. In 2014, he was honored as the National Distinguished Professor by Shandong University and currently works in the Institute of Space Sciences in Shandong University at Weihai. He is the author of GPS (2003, 2007 and 2016) and Orbits (2008 and 2013).